

Cite this: *Mater. Adv.*, 2026,  
7, 4329

# Exploring synergistic effects of a neodymium-based metal organic framework with SWCNTs and MXene for hybrid energy storage devices

Muhammad Shahbaz,<sup>a</sup> Shahzad Sharif,<sup>a</sup> Sidra Farid,<sup>a</sup>  
Muhamad Imran Din,<sup>b</sup> Zaib Hussain,<sup>b</sup> Khadija Nasir,<sup>a</sup> Reana Tajamal,<sup>a</sup>  
Soha Rafique,<sup>a</sup> Ayoub Rashid Ch<sup>a</sup> and Islam Ullah Khan<sup>b</sup>

Hybrid supercapacitors (HSCs) with high energy density and power density, along with an extended cycle life, have emerged as ultimate energy storage devices. Owing to their high redox activity, large surface area, porous topological framework, open topological structure, and configurable morphology, metal-organic frameworks (MOFs) have attracted substantial interest as electrode materials. However, they suffer from the problems of poor electrical conductivity and inadequate stability. Herein, a neodymium-based MOF derived from pyridine-2,6-dicarboxylic acid (Nd-PDA) and its composites with an MXene (Nd-PDA@MXene) and single-walled carbon nanotubes (Nd-PDA@SWCNT) were developed, and their applicability as electrode materials was analyzed through electrochemical characterizations. The electrochemical analysis displayed that the Nd-PDA@SWCNT composite exhibited superior electrochemical performance with an outstanding specific capacity ( $Q_s$ ) of 260.91 C g<sup>-1</sup> and specific capacitance ( $C_s$ ) of 521.82 F g<sup>-1</sup> at a current density of 1 A g<sup>-1</sup>. The Nd-PDA@SWCNT composite was integrated with activated carbon (AC) to design an HSC, which demonstrated a  $Q_s$  of 104.24 C g<sup>-1</sup> and a  $C_s$  of 69.49 F g<sup>-1</sup> (555.92 mF cm<sup>-2</sup>) at 0.5 A g<sup>-1</sup>. A maximum specific energy ( $E_s$ ) of 21.71 Wh kg<sup>-1</sup> and specific power ( $P_s$ ) of 1151 W kg<sup>-1</sup> with a Coulombic efficiency (CE) of 99% were determined even after 10 000 charging-discharging cycles. Dunn's method was employed to assess the capacitive and diffusive contributions. The findings indicate that the Nd-PDA@SWCNT composite is an outstanding electrode material for application in hybrid energy-storage devices.

Received 1st November 2025,  
Accepted 23rd March 2026

DOI: 10.1039/d5ma01269d

rsc.li/materials-advances

## 1. Introduction

In the recent past, hybrid supercapacitors (HSCs) have attracted much attention from researchers.<sup>1</sup> Numerous types of electrode materials have been reported to enhance the electrochemical performance of HSCs, which include conducting polymers, carbon-based materials,<sup>2</sup> transition metal oxides,<sup>3</sup> hydroxides,<sup>4</sup> phosphates,<sup>5</sup> phosphides,<sup>6</sup> sulfides,<sup>7</sup> and selenides,<sup>8</sup> and a new class of materials known as metal-organic frameworks (MOFs).<sup>9,10</sup> However, poor electrical conductivity and low structural stability hinder the practical applications of MOFs. To overcome these shortcomings and to exploit the full potential of MOFs, conductive materials have been employed.<sup>11-13</sup> Carbon nanotubes (CNTs) are among the most desirable carbon materials applied for energy

storage devices due to their remarkable conductivity, outstanding mechanical strength, exceptional chemical stability, high thermal conductivity, and large surface area.<sup>14,15</sup> Among CNTs, single-walled carbon nanotubes (SWCNTs) are exceptionally well-suited for energy storage applications due to their remarkable features.<sup>16</sup> SWCNTs possess exceptional mechanical, electrical, chemical, thermal, and optical properties.<sup>17</sup>

Rare-earth metal ions have gained considerable scientific interest as electrode materials due to their remarkable electrochemical performance.<sup>18,19</sup> Due to lanthanide contraction, Nd<sup>3+</sup> shows higher coordination numbers (usually 8-9) than transition metals, which are responsible for its robust 3D framework. It is evident that direct f-electron participation in redox processes is limited for Nd<sup>3+</sup>; hence, charge transfer through the organic linker is facilitated by its unique electronic structure. Nd<sup>3+</sup> can also stabilize oxygen vacancies, serving as active sites for reversible OH<sup>-</sup> adsorption/desorption.<sup>20</sup> Furthermore, an optimal ionic radius results in a highly porous structure with a large surface area. It can also act as a Lewis acid to enhance interaction with electrolyte ions.

<sup>a</sup> Materials Chemistry Laboratory, Institute of Chemical Sciences, Government College University Lahore, 54000, Pakistan. E-mail: mssharif@gcu.edu.pk; Tel: +92 345 4579334

<sup>b</sup> School of Chemistry, University of the Punjab, Lahore, Pakistan



Majumder *et al.* showcased that the PIn/Nd<sub>2</sub>O<sub>3</sub>-2 composite demonstrated a  $C_s$  of 401 F g<sup>-1</sup>, an  $E_s$  of 8.91 Wh kg<sup>-1</sup>, and a  $P_s$  of 1020 W kg<sup>-1</sup>, along with 97.02% retention after 5000 cycles.<sup>21</sup> Shiri *et al.* showed that the POAP/Nd<sub>2</sub>O<sub>3</sub> nanorod composite retained 92% of its initial capacitance after 1000 cycles and a  $C_s$  of 379 F g<sup>-1</sup>.<sup>22</sup> Imtiaz *et al.* developed the Nd-doped SmFeO<sub>3</sub> electrode and revealed that the two-electrode symmetric cell has a  $E_s$  of 4.3 Wh kg<sup>-1</sup> and a  $P_s$  of 722.5 W kg<sup>-1</sup>.<sup>23</sup> Sahu *et al.* revealed that the 3% Nd-doped ZnO electrode delivered a  $C_s$  of 154 F g<sup>-1</sup> at 2.5 A g<sup>-1</sup>, an  $E_s$  of 7.36 Wh kg<sup>-1</sup>, and a  $P_s$  of 730 W kg<sup>-1</sup>, with 92% capacity retention even after 1000 cycles at 2.5 A g<sup>-1</sup>.<sup>24</sup> The in-depth crystal engineering of Nd-MOFs obtained from a template-assisted approach signified the structural and magnetic relationship.<sup>25</sup> Nd-MOFs have also been reported for the reduction of CO<sub>2</sub> to syngas,<sup>26</sup> and the use of a rare-earth metal to design Zr-MOFs and their composites have also been highlighted for sensing and energy applications.<sup>27</sup> In most of the reported rare-earth MOFs, conventional carboxylic linkers were used, which showed poor conductivity.<sup>25</sup> However, our work revolves around the utilization of pyridine-2,6-dicarboxylic acid (PDA), where the lone pair on the nitrogen atom not only contributes to increasing the conductivity but also provides strong chelation with Nd<sup>3+</sup> through the carboxylate unit. Furthermore, the use of conductive materials has further unlocked the hidden electrochemical potential of the synthesized material.<sup>28,29</sup>

In this study, the Nd-PDA MOF with organic linker pyridine-2,6-dicarboxylic acid containing a nitrogen (N) atom was synthesized *via* sonication. After structural characterization *via* single-crystal X-ray diffraction (XRD), thermogravimetric analysis (TGA) and Fourier-transform infrared (FT-IR) spectroscopy, composites of the Nd-PDA MOF with MXene (Nd-PDA@MXene) and SWCNTs (Nd-PDA@SWCNT) were designed and electrochemically tested *via* cyclic voltammetry (CV), electrochemical impedance spectroscopy (EIS), and galvanostatic charge-discharge (GCD) measurements. The results showed that the addition of SWCNTs, owing to their remarkable electrical conductivity, substantial active sites, and ideal nano-tubular structure, enhanced the electrochemical performance. The Nd-PDA@SWCNT composite was fabricated in HSCs, which demonstrated significant potential for use as an electrode material in futuristic energy storage systems.

## 2. Experimental

### 2.1. Materials

Neodymium nitrate hexahydrate (Nd(NO<sub>3</sub>)<sub>2</sub>·6H<sub>2</sub>O), pyridine-2,6-dicarboxylic acid (PDA), distilled water, MXene (Ti<sub>3</sub>C<sub>2</sub>) with 99.9% purity, a single-walled carbon nanotube (SWCNT), *N*-methyl-2-pyrrolidone (NMP), polyvinylidene fluoride (PVDF), dimethylformamide (DMF), activated carbon (AC), hydrochloric acid (HCl), ethanol, nickel foam (NF), and potassium hydroxide (KOH) were the materials used in this study. All chemicals and reagents with analytical-grade purity were sourced from Sigma-Aldrich and used as received without additional purification.

### 2.2. Preparation of neodymium metal-organic framework (Nd-PDA MOF)

In order to synthesize Nd-PDA MOF, 131 mg (0.4 mM) of Nd(NO<sub>3</sub>)<sub>2</sub>·6H<sub>2</sub>O salt and 77 mg (0.4 mM) of PDA were dissolved separately in 2 mL of distilled water. After mixing, the solution was sonicated for 1 minute at a 12 μm amplitude. The resulting transparent solution was kept for crystallization. Purple crystals appeared after five days, which were then filtered, washed, and dried at room temperature (calc. for C<sub>21</sub>H<sub>13</sub>N<sub>3</sub>Nd<sub>2</sub>O<sub>16</sub> (851.82): N, 4.93; C, 30.82; H, 1.52; found: N, 4.63; C, 30.73; H, 1.60).

### 2.3. Electrode fabrication

To form a homogeneous slurry, 4 mg of Nd-PDA MOF, 0.5 mg of AC, and 0.5 mg of the PVDF binder were mixed with 60 μL of the NMP solvent. Likewise, composites such as Nd-PDA@MXene and Nd-PDA@SWCNT were prepared with the same ratio by utilizing conductive materials instead of AC. The mixture was stirred for 6 h at room temperature. NF (1.5 × 1.5 cm<sup>2</sup>) was conditioned by subsequent washing with 6 M HCl, distilled water, and ethanol to eliminate any oxide. Drop casting technique was employed to fabricate the materials on pre-treated NF to prepare electrodes (Nd-PDA, Nd-PDA@MXene and Nd-PDA@SWCNT), which were dried at 60 °C for 6 h (Fig. 1). The active mass loading was determined by measuring the weight difference of the NF substrate before and after electrode fabrication, which was approximately 3.8–4 mg cm<sup>-2</sup>.

### 2.4. Electrochemical tests

We conducted all the electrochemical experiments on the OrigaFlex electrochemical workstation. These tests included CV, GCD, and EIS. In a three-electrode assembly, the prepared electrodes served as the working electrodes, while platinum wire and Ag/AgCl electrodes served as reference and counter electrodes, respectively.<sup>30</sup> A hybrid supercapacitor was constructed using a two-electrode system. The positive electrode consisted of Nd-PDA@SWCNT, while the negative electrode was made from AC. The electrolyte used was 1 M KOH. The mass ratio between the electrodes was determined using eqn (1):<sup>9</sup>

$$\frac{m_+}{m_-} = \frac{C_{s-} \times \Delta V_-}{Q_s} \quad (1)$$

here,  $m_-$  is the loaded mass (g),  $\Delta V_-$  is the potential window, and  $C_{s-}$  is the specific capacitance of the negative electrode, while  $m_+$  and  $Q_s$  represent the loaded mass (g) and specific capacity of the positive electrode, respectively.

The  $Q_s$  and  $C_s$  values were determined from the GCD graphs using eqn (2) and (3), respectively. In the given equations,  $I$  is the discharge current (A),  $m$  denotes the loaded mass (g),  $\int V dt$  represents the current integral area, and  $\Delta V$  corresponds to the potential window (V).<sup>31</sup> Eqn (4) and (5) were used to calculate the  $E_s$  (Wh kg<sup>-1</sup>) and  $P_s$  (W kg<sup>-1</sup>), respectively. Here,  $t_d$  represents the discharge time, in seconds, taken from the GCD curve.<sup>32</sup>

$$Q_s = \frac{2 \times I \int V dt}{m \Delta V} \quad (2)$$



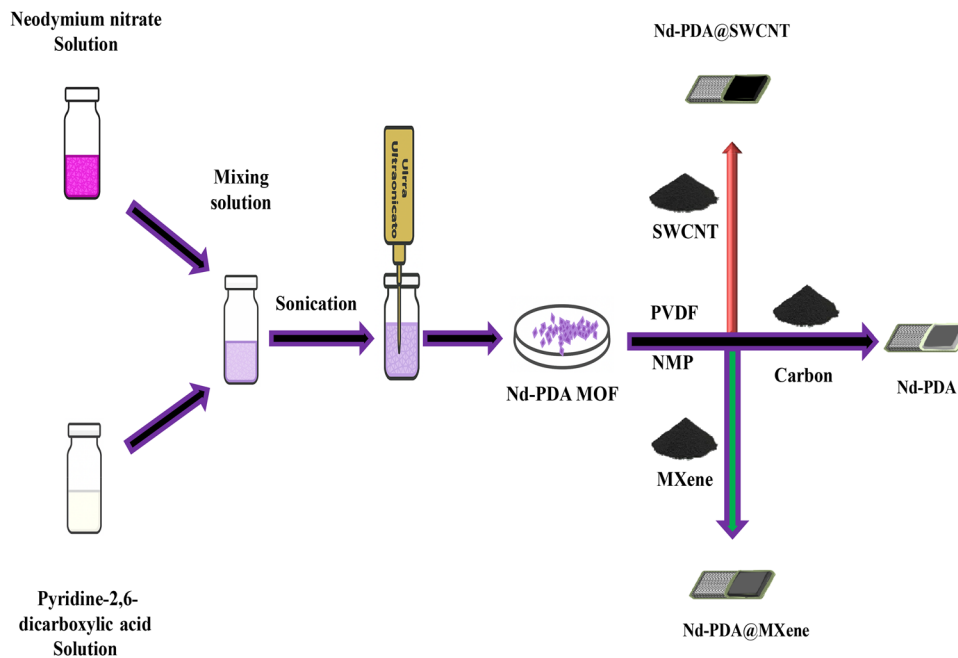


Fig. 1 Synthesis scheme of Nd-PDA MOF, Nd-PDA@MXene and Nd-PDA@SWCNT.

$$C_s = \frac{2 \times I \int V dt}{m \Delta V^2} \quad (3)$$

$$E_s = \frac{C_s \times \Delta V^2}{3.6} \quad (4)$$

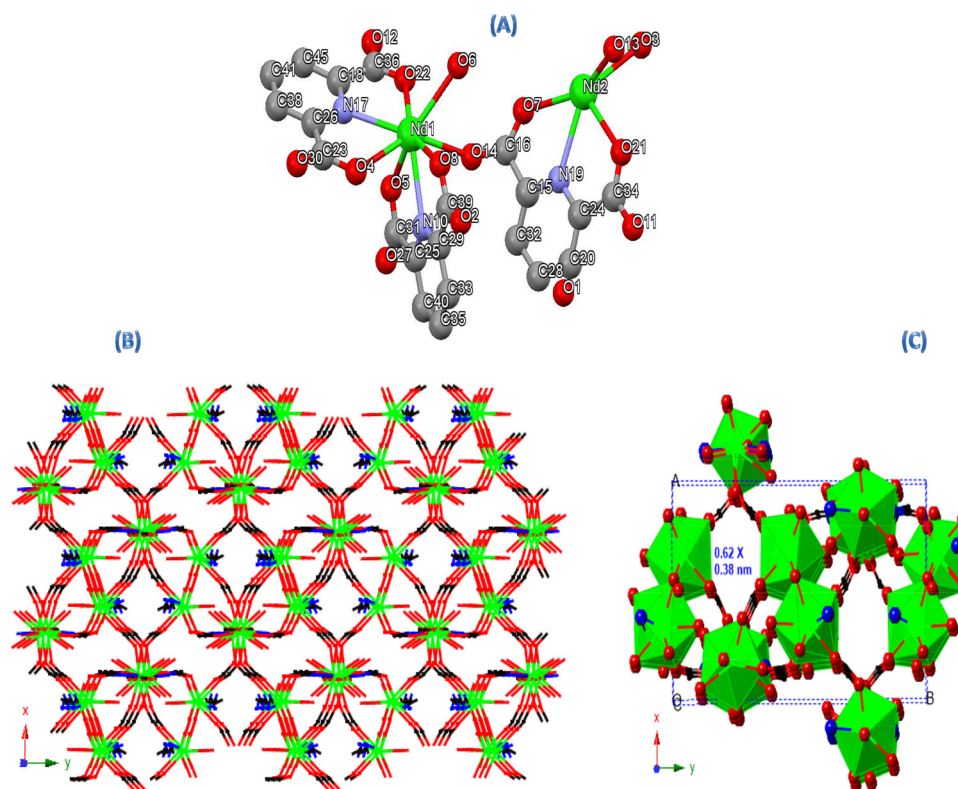


Fig. 2 (A) Asymmetric unit of the Ce-3D polymer; colour of atoms: magenta: cerium, blue: nitrogen, red: oxygen, black: carbon, and white: hydrogen. (B) Schematic stick view of 3D propagation along the 001 direction in the Ce-3D polymer. (C) Polyhedral view showing a spherical pore.



$$P_s = \frac{E \times 3600}{I_d} \quad (5)$$

### 3. Results and discussion

#### 3.1. Structural characterization

**3.1.1. Single-crystal X-ray diffraction analysis of Nd-PDA MOF.** At 296 K, a diffraction experiment was performed, and the procedures involved in this analysis are as follows: data collection: COLLECT,<sup>33</sup> cell refinement: DENZO/SCALEPACK,<sup>38</sup> and data reduction: DENZO/SCALEPACK. The program(s) used for molecular graphics were the Mercury programs.<sup>39</sup> The software used to prepare materials for publication was WinGX.<sup>34</sup> All non-hydrogen atoms were refined with anisotropic parameters.

**3.1.2. Description of structures.** The asymmetric unit of the Nd-PDA MOF consists of two Nd(III) ions, two coordinated and one non-coordinated water molecules, and three PDA ligands (Fig. 2A). The bond lengths and angles are similar to those of the reported structure,<sup>35</sup> and the Schematic stick view of the 3D propagation along 001 direction in the Nd-3D polymer is shown in Fig. 2B, while the polyhedral view showing a rectangular pore of  $6.2 \times 3.8$  nm is shown in Fig. 2C. Details of crystal structures and selected bond lengths and angles are

given in Tables S1 and S2, respectively. A simulated XRD diffractogram of Nd-PDA MOF is presented in Fig. S1.

**3.1.3. Thermogravimetric analysis (TGA) and Fourier transform infrared (FTIR) spectroscopy.** TGA was carried out on TA Instruments with a ramp rate of  $10 \text{ }^\circ\text{C min}^{-1}$  using an SDT Q 600 instrument thermal analyzer under an  $\text{N}_2$  atmosphere in a temperature range of  $25 \text{ }^\circ\text{C}$  to  $1000 \text{ }^\circ\text{C}$ . The decomposition pattern of the complex ND-PDA MOF is illustrated in Fig. S2. At the first stage, water was released with a weight loss of about 6.3% (calculated value is 6.4%) for two coordinated water molecules and one non-coordinated water molecule up to  $182 \text{ }^\circ\text{C}$ . The TGA curve exhibits a gradual mass loss up to  $988 \text{ }^\circ\text{C}$  due to the successive decomposition of the polymer to release PDA, leaving a 46.3% residue attributed to  $\text{Nd}_2\text{O}_3$  (the calculated value is 39.4%). The slight variation in the experimental and theoretical residue amounts may be due to the presence of carbon.

FTIR spectrum was measured using the ATR sample compartment on the Bruker Tensor-27 spectrophotometer (Billerica, MA, USA) in the range of  $400\text{--}4000 \text{ cm}^{-1}$ . The asymmetric and symmetric stretching vibrations associated with the carboxylic group at  $1673 \text{ cm}^{-1}$  and  $1352 \text{ cm}^{-1}$  confirmed the coordination of the  $\text{Nd}^{3+}$  ions. The peaks at  $1511 \text{ cm}^{-1}$  correspond to the C=C stretching of the pyridine ring, whereas the broad band at  $3212 \text{ cm}^{-1}$  indicates the presence of water molecules (Fig. S3).

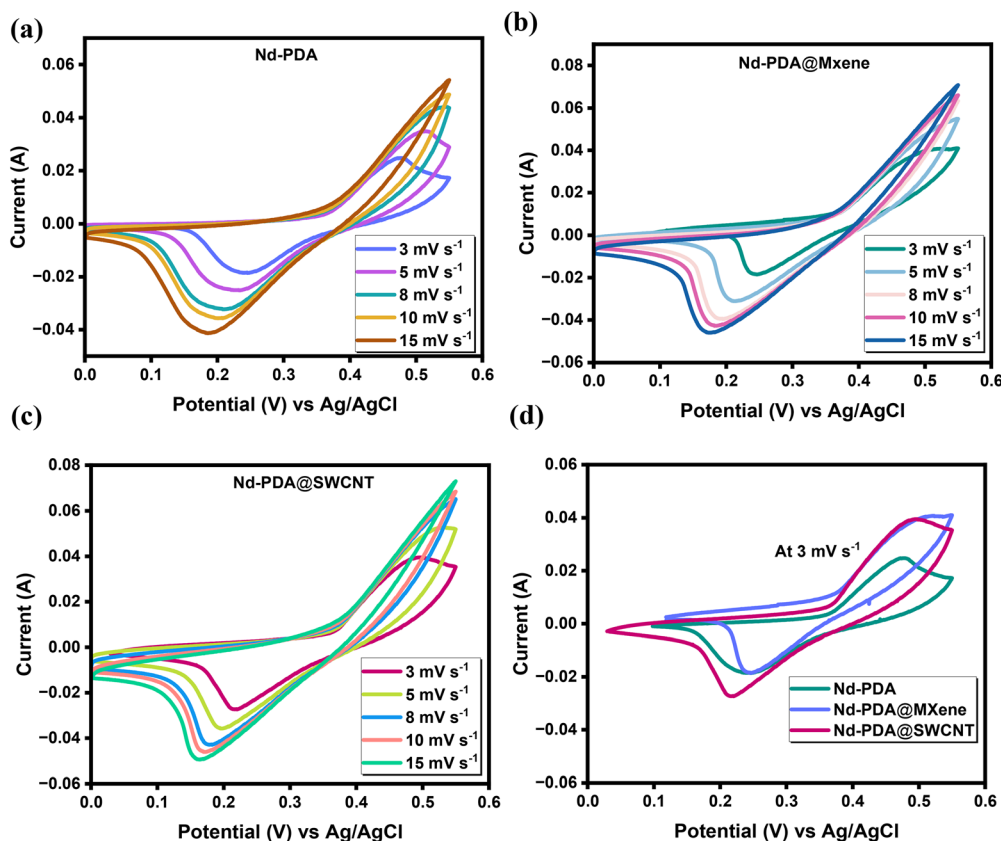


Fig. 3 Electrochemical performance of Nd-PDA, Nd-PDA@MXene, and Nd-PDA@SWCNT in a three-electrode assembly. Cyclic voltammograms of (a) Nd-PDA, (b) Nd-PDA@MXene, and (c) Nd-PDA@SWCNT. (d) Comparison of the CV curves for Nd-PDA, Nd-PDA@MXene, and Nd-PDA@SWCNT at  $3 \text{ mV s}^{-1}$ .



### 3.2. Electrochemical characterization

#### 3.2.1. Half-cell electrochemical characterization

**3.2.1.1. Cyclic voltammetry (CV) analysis.** CV is a widely utilized electroanalytical method for determining the kinetics and nature of electrochemical processes.<sup>36,37</sup> It reveals details regarding the redox response of electroactive materials, the rate of heterogeneous electron transport reactions, the nature of the material, and linked chemical and electrochemical reactions.<sup>38</sup> The electrochemical performance of the as-prepared electrodes was first assessed by CV at different scan rates (3, 5, 8, 10, and 15  $\text{mV s}^{-1}$ ). Fig. 3a–c illustrates the CV plots of the Nd-PDA MOF, Nd-PDA@MXene, and Nd-PDA@SWCNT composite electrodes at a potential range of 0–0.55 V. The voltammograms of all three electrodes revealed redox peaks depicting the characteristics of faradaic redox reactions. The reduction of  $\text{Nd}^{3+}$  to  $\text{Nd}^{2+}$  in an aqueous alkaline electrolyte is not thermodynamically favourable, and the charge-storage mechanism can generally be associated with the high oxophilicity of  $\text{Nd}^{3+}$  that can stabilize oxygen vacancies serving as active sites for reversible  $\text{OH}^-$  adsorption/desorption.<sup>20</sup> Furthermore, a conjugated

system is created due to the coordination of PDA with  $\text{Nd}^{3+}$ , which is responsible for delocalization. Nd serves as a structural node for organizing redox-active ligands into accessible frameworks.<sup>39</sup> It is worth noting that the peak current increased with the augmentation of scan rates.<sup>40</sup> The elevated scan rate altered the oxidation and reduction voltages to relatively high positive and negative potentials, owing to the inherent resistance of the electrode material.<sup>41</sup> The redox peaks close to each other suggested an increase in catalytic activity. At relatively high scan rates, a shift in peak was observed, which indicated that the electroactive ions lacked enough time to integrate into the pores for redox activity.<sup>42</sup>

A comparison of the CV curves for all the prepared samples at a scan rate of 3  $\text{mV s}^{-1}$  is presented in Fig. 3d, which revealed that the Nd-PDA@SWCNT electrode had the highest CV area, confirming the greatest charge storage capacity due to enriched electrochemical kinetics.<sup>41</sup> The Nd-PDA MOF, Nd-PDA@MXene, and Nd-PDA@SWCNT electrodes' charge-storage responses were verified from CV graphs using a power law (eqn (6) and (7)).

$$i = av^b \quad (6)$$

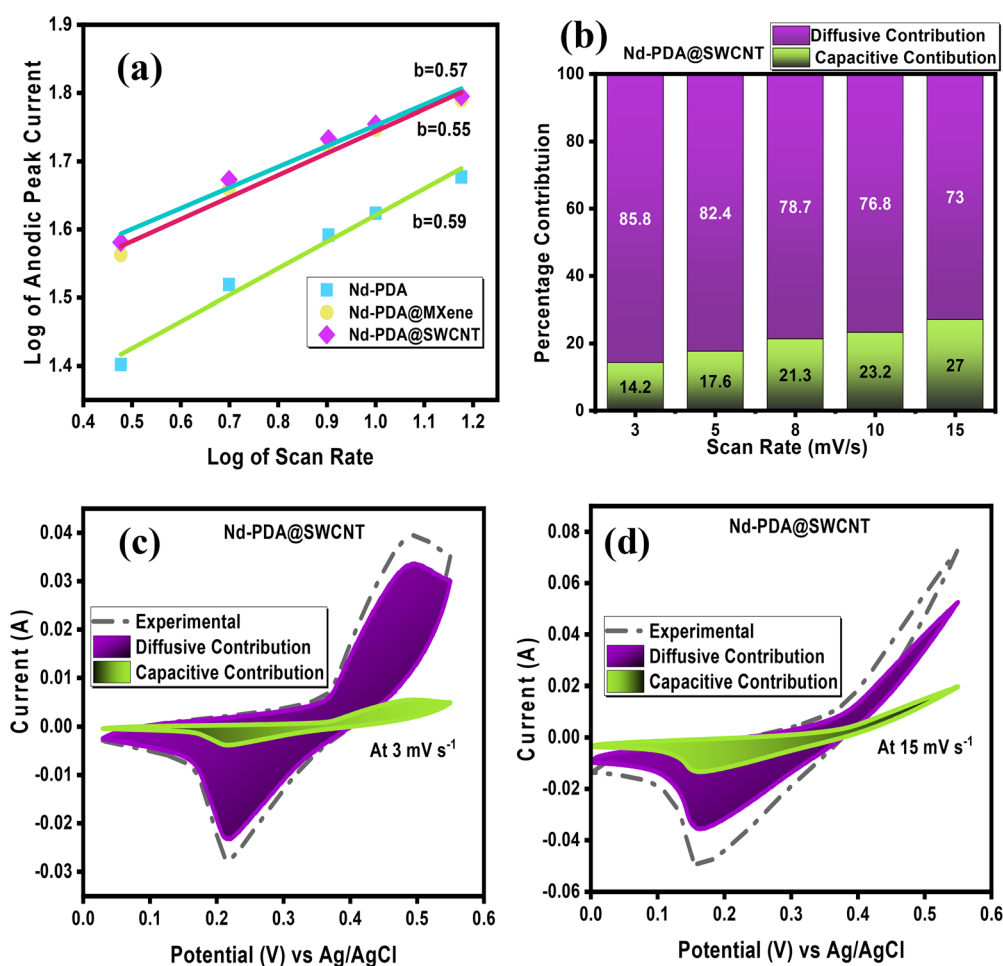


Fig. 4 (a) Comparison of the  $b$ -values for Nd-PDA, Nd-PDA@MXene, and Nd-PDA@SWCNT. (b) Bar chart showing the diffusive and capacitive contributions (in percentage) at various scan rates for Nd-PDA@SWCNT. Comparison of the diffusive-d capacitive-regulated contributions for Nd-PDA@SWCNT at (c) 3  $\text{mV s}^{-1}$  and (d) 15  $\text{mV s}^{-1}$ .



$$\log(i) = \log(a) + b \log(v) \quad (7)$$

where  $i$  is the peak current value,  $v$  is the scan rate, and  $a$  and  $b$  are constants that can be adjusted. The slope of the linear line can be used to determine the  $b$ -value, which helps to distinguish between surface-controlled (capacitive) and diffusion-controlled (battery-like) processes. Particularly, a  $b$ -value of 0.5 suggests a diffusion-controlled process, while a  $b$ -value close to 1 suggests a surface-controlled capacitive process. The hybrid storage system comprising diffusion-controlled and surface-regulated mechanisms falls at around 0.8.<sup>43</sup> The linear plots of  $\log(i)$  vs.  $\log(v)$  for the Nd-PDA, Nd-PDA@MXene, and Nd-PDA@SWCNT electrodes are

depicted in Fig. 4a. The  $b$ -values for Nd-PDA, Nd-PDA@MXene, and Nd-PDA@SWCNT were found to be 0.59, 0.55, and 0.57, indicating that the charge storage was primarily accomplished through a diffusion-regulated electrochemical process.

In addition, the Dunn's method was applied to quantify the contribution of the capacitive and the diffusion mechanisms, by applying eqn (8) and (9).<sup>44</sup>

$$i(V) = k_1 v + k_2 v^{1/2} \quad (8)$$

$$\left(\frac{i(V)}{v^{1/2}}\right) = k_1 v^{1/2} + k_2 v^{1/2}, \quad (9)$$

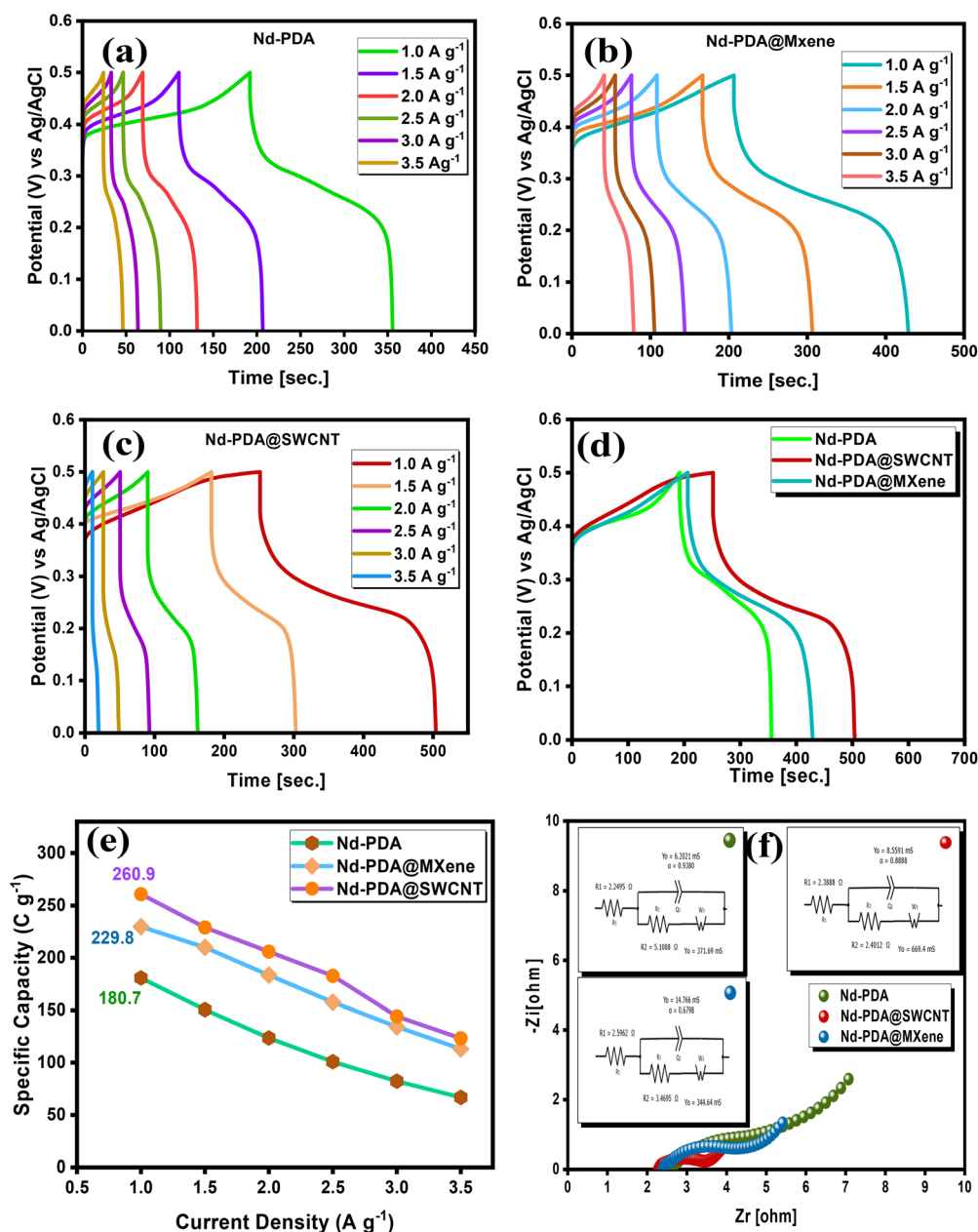


Fig. 5 GCD profiles of (a) Nd-PDA, (b) Nd-PDA@MXene, and (c) Nd-PDA@SWCNT. (d) Comparison of the GCD curves of Nd-PDA, Nd-PDA@MXene, and Nd-PDA@SWCNT at 1 A g<sup>-1</sup>. (e)  $Q_s$  of Nd-PDA, Nd-PDA@MXene, and Nd-PDA@SWCNT at different current densities. (f) Evaluation of the fitted curves and comparison of the electrochemical impedance spectra of Nd-PDA, Nd-PDA@MXene, and Nd-PDA@SWCNT.



where  $i(V)$  is the current at a specific voltage  $V$ ,  $\nu$  represents the scan rate, and  $k_1\nu$  and  $k_2\nu^{1/2}$  signify capacitive- and diffusion-controlled current, respectively. Furthermore, the values of  $k_1$  and  $k_2$  can be acquired from the slope and intercept of the fitted plot between  $i(V)/\nu^{1/2}$  and  $\nu^{1/2}$ , respectively.<sup>45</sup> The diffusive and capacitive contributions of Nd-PDA@SWCNT at scan rates of  $3 \text{ mV s}^{-1}$  to  $5 \text{ mV s}^{-1}$  are illustrated in Fig. 4b. The diffusion-controlled contribution of Nd-PDA@SWCNT at a scan rate of  $5 \text{ mV s}^{-1}$  (Fig. 4c) made up about 85.8% of the total current, which decreased to 73% at a scan rate of  $15 \text{ mV s}^{-1}$  (Fig. 4d), demonstrating that the diffusion-regulated process still dominates the overall capacitance of Nd-PDA@SWCNT.

**3.2.1.2. Galvanostatic charge–discharge (GCD) measurements.** GCD is a crucial instrument for determining the key parameters

pertaining to the electrochemical characteristics of materials, including  $Q_s$ ,  $C_s$ ,  $P_s$ , and  $E_s$ .<sup>46,47</sup> It is easy to study the kinetics of charge transfer and ion diffusion in different electrode materials using GCD because voltage and current fluctuations are applied continuously to the electrode and monitored over time.<sup>48</sup> The GCD curves of Nd-PDA MOF, Nd-PDA@MXene, and Nd-PDA@SWCNT in the voltage window of 0.0 to 0.5 V, with various current densities ranging from 1.0 to  $3.5 \text{ A g}^{-1}$ , are shown in Fig. 5a–c. The non-linear profile and humps in the GCD curves confirmed the battery-like nature of all the materials. The GCD curves of Nd-PDA MOF, Nd-PDA@MXene, and Nd-PDA@SWCNT at a current density of  $1 \text{ A g}^{-1}$  (Fig. 5d) revealed that Nd-PDA@SWCNT had the longest discharge duration. The values of  $C_s$  and  $Q_s$  were obtained at various current densities (1 to  $3.5 \text{ A g}^{-1}$ ) using eqn (2) and (3). Nd-PDA

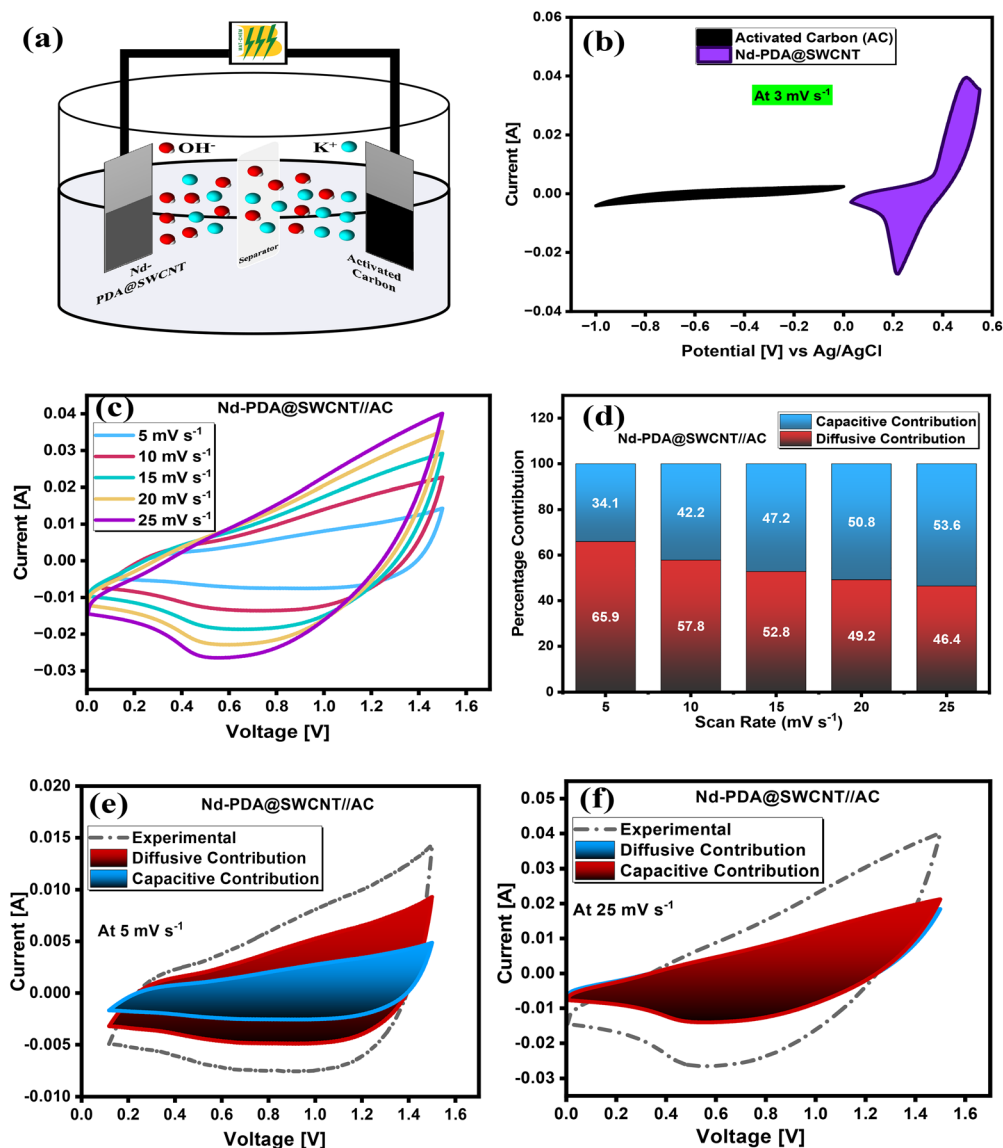


Fig. 6 Electrochemical characteristics of the Nd-PDA@SWCNT hybrid device. (a) Illustrative diagram of the hybrid system. (b) CV profiles of the Nd-PDA@SWCNT in conjunction with AC. (c) CV profiles of the Nd-PDA@SWCNT//AC hybrid device at various scan rates. (d) Bar chart showing the diffusive and capacitive contributions (in percentage) at different scan rates. Comparison of the diffusive and capacitive-regulated contributions at (e)  $5 \text{ mV s}^{-1}$  and (f)  $25 \text{ mV s}^{-1}$ .



MOF, Nd-PDA@MXene, and Nd-PDA@SWCNT showed  $Q_s$  values of 180.73, 229.77, and 260.91  $C g^{-1}$  at  $1 A g^{-1}$ , respectively. The comparison of the  $Q_s$  for all the materials is shown in Fig. 5e. Furthermore, the  $C_s$  values for Nd-PDA, Nd-PDA@MXene, and Nd-PDA@SWCNT were determined as 361.47, 459.54, and 521.82  $F g^{-1}$  at  $1 A g^{-1}$ , respectively. It is essential to recognize that the values of  $Q_s$  and  $C_s$  decreased with increased current density due to the limited utilization of active material.<sup>40</sup> The enhanced performance of Nd-PDA@SWCNT is associated with SWCNT-mediated improvements in electrochemical reaction kinetic and charge transport.

**3.2.1.3. Electrochemical impedance spectroscopy (EIS).** EIS was employed to assess the intrinsic impedance, charge-transport

resistance, electrolyte dispersion, and ion diffusion features of the materials.<sup>45</sup> In the three-electrode system, the EIS measurements were conducted across a frequency range of 0.1 Hz to 100 kHz. The Nyquist curves with the equivalent circuit modeling obtained for the Nd-PDA MOF, Nd-PDA@MXene, and Nd-PDA@SWCNT electrodes are displayed in Fig. 5f. The Nyquist maps depict the relationship between the real part of the impedance ( $Z$ ) and imaginary part of the impedance ( $-Z$ ). They offer a deeper understanding of the resistive and capacitor-like characteristics of the electrode materials. The EIS curve for a battery-like material is generally composed of a small semi-circle and a straight line. A vertical line in the area of low frequency represents the Warburg resistance ( $Z_w$ ), which is

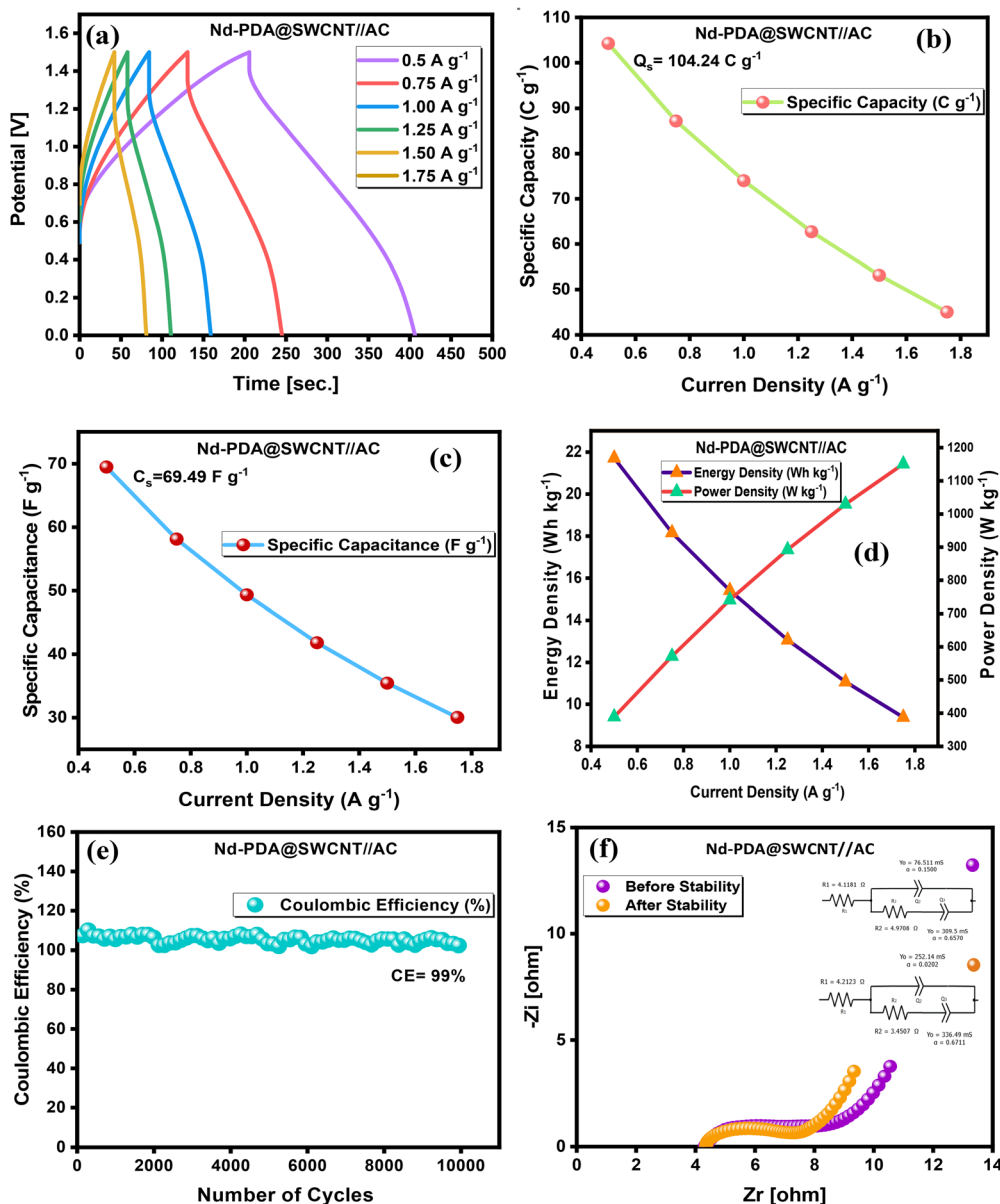


Fig. 7 (a) GCD profiles at varying current densities, (b) specific capacities plotted at varying current densities, (c) specific capacitance values at various current densities, (d) graph of specific energy and specific power at different current densities, (e) stability curve following 10 000 GCD cycles of the Nd-PDA@SWCNT//AC hybrid system, and (f) EIS spectrum taken before and after the stability test.



associated with the diffusion of ions in the electrolyte and their transport to the electrode. The semicircular diameter in the area of high frequency is related to charge-transfer resistance ( $R_{ct}$ ), which is linked to the faradaic reactions occurring at the electrolyte-electrode interface.<sup>49</sup> The resistance associated with the ionic conductivity of the electrolyte is the solution resistance ( $R_s$ ). It can be determined from the convergence with the actual axis in the high-frequency area.<sup>50</sup> The Nd-PDA@SWCNT electrode exhibited an  $R_s$  value of 2.3  $\Omega$ , which is lower than that of Nd-PDA@MXene (2.5  $\Omega$ ) but moderately higher than that of the Nd-PDA electrode (2.2  $\Omega$ ), implying that Nd-PDA@SWCNT has reasonable conductivity. The  $R_{ct}$  of the Nd-PDA@SWCNT electrode measured from the semicircle was 2.4  $\Omega$ , which was much smaller than that of the Nd-PDA@MXene (3.4  $\Omega$ ) and Nd-PDA MOF (5.1  $\Omega$ ). It confirmed a high electrical conductivity and quick charge transport kinetics. This finding revealed that the electrochemical resistance of the Nd-PDA electrode can be reduced by incorporating an SWCNT. The Nd-PDA@SWCNT electrode exhibited a more prominently inclined line in the low-frequency area as compared to the Nd-PDA@MXene and Nd-PDA electrodes, suggesting enhanced transportation of ions in the electrode materials, as well as reduced Warburg resistance.

**3.2.2. Hybrid supercapacitor assembly.** It is evident from the three-electrode assembly that the Nd-PDA@SWCNT possessed superior electrochemical performance owing to the coordinated interaction between the Nd-PDA MOF and SWCNT. A hybrid supercapacitor (HSC) was fabricated using Nd-PDA@SWCNT as the cathode and AC as the anode, segregated by a Whatman filter paper as a separator in 1 M KOH, as presented in Fig. 6a. The voltage of the HSC was assessed as 1.5 V from the CV curves of Nd-PDA@SWCNT and AC (Fig. 6b). The CV profiles of the HSC at different scan rates (5 to 25  $\text{mV s}^{-1}$ ) depicted a pseudo-capacitive nature involved in charge storage (Fig. 6c). The value of  $R^2$  around 0.99 confirmed the excellent reversibility of the device (Fig. S4). The calculated  $b$ -value of 0.67 confirmed charge storage through both diffusive/capacitive processes (Fig. S5), implying the hybrid character of the device. The diffusive and capacitive contributions measured at scan rates ranging from 5 to 25  $\text{mV s}^{-1}$  are depicted in Fig. 6d. The capacitive contribution of HSC was found to be 34.1% at 5  $\text{mV s}^{-1}$ , which increased to 53.6% at 25  $\text{mV s}^{-1}$ . At relatively high scan rates, the capacitive-regulated contributions became more dominant due to the predominance of the surface-charge storage mechanism.<sup>51</sup> The contributions of capacitive and diffusive currents at scan rates of 5  $\text{mV s}^{-1}$  and 25  $\text{mV s}^{-1}$  are shown in Fig. 6e and f.

To evaluate the practical application of the HSC, GCD was performed at current densities varying from 0.5 to 1.75  $\text{A g}^{-1}$ , with a potential window of 0.0–1.5 V (Fig. 7a). The appearance of the humps in the curves signified a combination of diffusive and capacitive contributions. The HSC showed  $Q_s$  and  $C_s$  values of 104.24  $\text{C g}^{-1}$  and 69.49  $\text{F g}^{-1}$  (555.92  $\text{mF cm}^{-2}$ ) at a current density of 0.5  $\text{Ag}^{-1}$ , respectively (Fig. 7b and c). The relationship between the  $E_s$  and  $P_s$  is also shown in Fig. 7d. The Nd-PDA@SWCNT//AC exhibited a high  $E_s$  of 21.71  $\text{Wh kg}^{-1}$  at 0.5  $\text{Ag}^{-1}$

**Table 1** Comparison of the performance of Nd-PDA@SWCNT with some reported Nd-based materials

Material	$E_s$ ( $\text{Wh kg}^{-1}$ )	$P_s$ ( $\text{W kg}^{-1}$ )	CE/CS (%)	Ref.
PIn/Nd <sub>2</sub> O <sub>3</sub> -2	8.91	1020	99.98	21
Nd/MnTiO <sub>3</sub>	14.2	3006	—	52
Nd-doped SmFeO <sub>3</sub>	4.3	722.5	—	23
Nd-doped ZnO3E	7.36	730	92	24
NdCrO <sub>3</sub> /GO	18	257	97.6	53
La <sub>0.85</sub> Nd <sub>0.15</sub> NiO <sub>3</sub>	7.3614	1076.2	—	54
Ni-CoP@C	17.4	699.1	76.1	55
MOF-CNT	23.6	501.5	79.1	56
Zr-MOF-CNT	17.53	902.5	—	57
Nd-PDA@SWCNT	21.71	1151	99	This work

and a  $P_s$  of 1151  $\text{W kg}^{-1}$  at 1.75  $\text{Ag}^{-1}$ . The device was run for 10 000 GCD cycles, which demonstrated a Coulombic efficiency of 99% (Fig. 7e). EIS was also performed before and after running 10 000 GCD cycles, and Randle's circuits were used to assess the kinetics of the charge-storage mechanism (Fig. 7f). After stability, the device showed a value of 3.45  $\Omega$  for  $R_{ct}$ . The results showed that Nd-PDA@SWCNT can be a promising candidate for use in hybrid supercapacitors.

## 4. Conclusions

In this work, the Nd-PDA MOF was prepared through a simple sonication method, and its composites, Nd-PDA@SWCNT and Nd-PDA@MXene, were designed to explore the electrochemical performance of HSCs. Our findings demonstrated that Nd-PDA@SWCNT exhibited superior performance in the three-electrode assembly with a  $Q_s$  of 260.91  $\text{C g}^{-1}$  and a  $C_s$  of 521.82  $\text{F g}^{-1}$  at 1  $\text{A g}^{-1}$ . Consequently, Nd-PDA@SWCNT was employed with AC to construct a hybrid supercapacitor (Nd-PDA@SWCNT//AC), which demonstrated a  $Q_s$  of 104.24  $\text{C g}^{-1}$  and a  $C_s$  of 69.49  $\text{F g}^{-1}$  (555.92  $\text{mF cm}^{-2}$ ) at 0.5  $\text{A g}^{-1}$ . Furthermore, the device achieved an  $E_s$  of 21.71  $\text{Wh kg}^{-1}$  and a  $P_s$  of 1151  $\text{W kg}^{-1}$ , with an outstanding Coulombic efficiency of 99% even after 10 000 GCD cycles. Undoubtedly, the values of  $P_s$  and  $E_s$  are moderate as compared to those for the state-of-the-art hybrid supercapacitors; however, they are quite competitive among rare-earth materials (Table 1). The constructed HSC showed exceptional cycle stability (99%), which is very crucial for practical applications. Furthermore, a  $P_s$  of 1151  $\text{W kg}^{-1}$  indicates a high rate capability, presenting the device as suitable for rapid charge/discharge. In the future, the electrode optimization will be focused on exploring high-voltage electrolytes in order to further enhance electrochemical attributes.

## Author contributions

Shahbaz: writing original draft, Shahzad: writing – review & editing, Sidra: characterization, Imran: methodology, Zaib: investigation, Khadija: formal analysis, Reana: synthesis, Soha: validation, Ayoub: data curation, Islam Ullah: review.



## Conflicts of interest

The authors declared that they have no competing interests.

## Abbreviations

PDA	Pyridine-3,5-dicarboxylic acid
SXRD	Single X-ray diffraction
NF	Nickel foam
PVDF	Polyvinylidene fluoride
NMP	N-methyl pyrrolidone
CV	Cyclic voltammetry
GCD	Galvanostatic charge–discharge
EIS	Electronic impedance spectroscopy
EDLC	Electric double layer capacitor
$C_s$	Specific capacitance
$Q_s$	Specific capacity
ESR	Equivalent series resistance
$R_{ct}$	Charge transfer resistance
$E_s$	Specific energy
$P_s$	Specific power

## Data availability

Data will be made available on request.

Supplementary information (SI) is available. See DOI: <https://doi.org/10.1039/d5ma01269d>.

CCDC 2497615 contains the supplementary crystallographic data for this paper.<sup>58</sup>

## References

- D.-G. Wang, Z. Liang, S. Gao, C. Qu and R. Zou, Metal-organic framework-based materials for hybrid supercapacitor application, *Coord. Chem. Rev.*, 2020, **404**, 213093, DOI: [10.1016/j.ccr.2019.213093](https://doi.org/10.1016/j.ccr.2019.213093).
- S. Mandal, A. B. Mendhe, H. M. Rakhade, N. S. Barse, M. Roy, P. Rosaiah, T. Park, H.-S. Lee, A. C. Mendhe and D. Kim, Recent advancement and design in supercapacitor hybrid electrode materials: Bridging the gap between energy and power density, *Chem. Eng. J. Adv.*, 2025, **21**, 100690, DOI: [10.1016/j.ceja.2024.100690](https://doi.org/10.1016/j.ceja.2024.100690).
- X. Zhu, Recent advances of transition metal oxides and chalcogenides in pseudo-capacitors and hybrid capacitors: A review of structures, synthetic strategies, and mechanism studies, *J. Energy Storage*, 2022, **49**, 104148, DOI: [10.1016/j.est.2022.104148](https://doi.org/10.1016/j.est.2022.104148).
- Z. Lu, Z. Hu, L. Xiao, Y. Xie, N. Li, L. Xi, W. Chen, J. Xiao and Y. Zhu, Battery-type Ni-Co-Se hollow microspheres cathode materials enabled by bifunctional N-doped carbon quantum dots with ultrafast electrochemical kinetics for hybrid supercapacitors, *Chem. Eng. J.*, 2022, **450**, 138347, DOI: [10.1016/j.cej.2022.138347](https://doi.org/10.1016/j.cej.2022.138347).
- A. M. Abkharaki and A. A. Ensafi, Phosphorus heteroatom doped in NiMn@CuO/CF as transition metal phosphide materials for hybrid supercapacitor, *J. Energy Storage*, 2024, **98**, 112953, DOI: [10.1016/j.est.2024.112953](https://doi.org/10.1016/j.est.2024.112953).
- S. Xie and J. Gou, Facile synthesis of Ni<sub>2</sub>P/Ni<sub>12</sub>P<sub>5</sub> composite as long-life electrode material for hybrid supercapacitor, *J. Alloys Compd.*, 2017, **713**, 10–17, DOI: [10.1016/j.jallcom.2017.04.170](https://doi.org/10.1016/j.jallcom.2017.04.170).
- X. Du, Z. Lin, X. Wang, K. Zhang, H. Hu and S. Dai, Electrode Materials, Structural Design, and Storage Mechanisms in Hybrid Supercapacitors, *Molecules*, 2023, **28**(17), 6432, DOI: [10.3390/molecules28176432](https://doi.org/10.3390/molecules28176432).
- X. Liu, Y. Zhu, Z. Lu, J. Xiao, G. Zou, H. Hou and X. Ji, Heterostructured flower-like NiO/Co<sub>3</sub>O<sub>4</sub> microspheres modified by bifunctional carbon quantum dots as a battery-type cathode for high energy and power density hybrid supercapacitors, *Carbon Neutralization*, 2023, **2**(6), 721–737, DOI: [10.1002/cnl2.97](https://doi.org/10.1002/cnl2.97).
- M. I. Khan, S. Alam, M. Z. Iqbal, N. Badi, M. R. Karim and A. Dahshan, Exploring the electrochemical synergy of metal sulfides and metal-organic framework composite as hybrid supercapacitor electrodes, *J. Alloys Compd.*, 2024, **1004**, 175750, DOI: [10.1016/j.jallcom.2024.175750](https://doi.org/10.1016/j.jallcom.2024.175750).
- M. Shahbaz, M. Saeed, S. Sharif, T. T. R. Afzal, A. Ashraf, B. Riaz, Z. Ghaznavi, S. Shahzad, M. W. Mushtaq and A. Shahzad, A Review on Architecting Rationally Designed Metal-Organic Frameworks for the Next-Generation Li-S Batteries, *Small*, 2025, **21**, 2406613, DOI: [10.1002/smll.202406613](https://doi.org/10.1002/smll.202406613).
- Q. Wang, Q. Wang, B. Xu, F. Gao, F. Gao and C. Zhao, Flower-shaped multiwalled carbon nanotubes@nickel-trimesic acid MOF composite as a high-performance cathode material for energy storage, *Electrochim. Acta*, 2018, **281**, 69–77, DOI: [10.1016/j.electacta.2018.05.159](https://doi.org/10.1016/j.electacta.2018.05.159).
- S. Sharif, J. H. Shah, M. Shahbaz, B. Riaz, S. Shahzad, A. Shahzad, O. Şahin, H. Ahmad and E. A. Al-Ammar, Structural, DFT and redox activity investigation of 2D silver based MOF for energy storage devices, *J. Electroanal. Chem.*, 2024, **961**, 118226, DOI: [10.1016/j.jelechem.2024.118226](https://doi.org/10.1016/j.jelechem.2024.118226).
- M. Shahbaz, S. Sharif, A. Shahzad, Z. S. Şahin, B. Riaz and S. Shahzad, Enhanced electrochemical performance of cerium-based metal organic frameworks derived from pyridine-2,4,6-tricarboxylic acid for energy storage devices, *J. Energy Storage*, 2024, **88**, 111463, DOI: [10.1016/j.est.2024.111463](https://doi.org/10.1016/j.est.2024.111463).
- F. Farbod, M. Mazloum-Ardakani, H. R. Naderi, A. Mirvakili, M. Wang, D. V. Shinde, S. Dante, P. Salimi, S. Lauciello and M. Prato, Indium based metal-organic framework/carbon nanotubes composite as a template for In<sub>2</sub>O<sub>3</sub> porous hexagonal prisms/carbon nanotubes hybrid structure and their application as promising super-capacitive electrodes, *J. Energy Storage*, 2022, **51**, 104238, DOI: [10.1016/j.est.2022.104238](https://doi.org/10.1016/j.est.2022.104238).
- R. K. Nare, S. Ramesh, V. Kakani, Y. Haldorai, C. Karthikeyan, B. P. Kumar, N. Siva Kumar, M. Asif, S. N. Kumar, D. P. Babu, K. R. Reddy and V. R. Pasupuleti, CNTs supported NiCo<sub>2</sub>O<sub>4</sub> nanostructures as advanced composite for high performance supercapacitors, *Diam. Relat. Mater.*, 2024, **141**, 110660, DOI: [10.1016/j.diamond.2023.110660](https://doi.org/10.1016/j.diamond.2023.110660).



- 16 S. Ryan, M. P. Browne, A. Zhussupbekova, D. Spurling, L. McKeown, D. Douglas-Henry, L. Prendeville, S. Vaesen, W. Schmitt, I. Shvets and V. Nicolosi, Single walled carbon nanotube functionalisation in printed supercapacitor devices and shielding effect of Tin(II) Oxide, *Electrochim. Acta*, 2023, **448**, 142168, DOI: [10.1016/j.electacta.2023.142168](https://doi.org/10.1016/j.electacta.2023.142168).
- 17 M. S. Lal, R. Badam, N. Matsumi and S. Ramaprabhu, Hydrothermal synthesis of single-walled carbon nanotubes/TiO<sub>2</sub> for quasi-solid-state composite-type symmetric hybrid supercapacitors, *J. Energy Storage*, 2021, **40**, 102794, DOI: [10.1016/j.est.2021.102794](https://doi.org/10.1016/j.est.2021.102794).
- 18 R. Siddiqui, M. Rani, A. Ahmad Shah, A. Razaq, R. Iqbal, R. Neffati and M. Arshad, Fabrication of tricarboxylate-neodymium metal organic frameworks and its nanocomposite with graphene oxide by hydrothermal synthesis for a symmetric supercapacitor electrode material, *Mater. Sci. Eng. B*, 2023, **295**, 116530, DOI: [10.1016/j.mseb.2023.116530](https://doi.org/10.1016/j.mseb.2023.116530).
- 19 S. Arunachalam, B. Kirubasankar, D. Pan, H. Liu, C. Yan, Z. Guo and S. Angaiah, Research progress in rare earths and their composites based electrode materials for supercapacitors, *Green Energy Environ.*, 2020, **5**(3), 259–273, DOI: [10.1016/j.gee.2020.07.021](https://doi.org/10.1016/j.gee.2020.07.021).
- 20 H. Cheng, Y. Guan, F.-P. Wang, T. Yang, L. Huang, J. Tang and R. Hu, Oxygen-vacancies-rich CeO<sub>x</sub>/TbCoP nanoparticles for enhanced electrocatalytic oxygen evolution reaction, *J. Alloys Compd.*, 2024, **972**, 172820, DOI: [10.1016/j.jallcom.2023.172820](https://doi.org/10.1016/j.jallcom.2023.172820).
- 21 M. Majumder, R. B. Choudhary, A. K. Thakur, C. S. Rout and G. Gupta, Rare earth metal oxide (RE<sub>2</sub>O<sub>3</sub>; RE = Nd, Gd, and Yb) incorporated polyindole composites: gravimetric and volumetric capacitive performance for supercapacitor applications, *New J. Chem.*, 2018, **42**(7), 5295–5308, DOI: [10.1039/C8NJ00221E](https://doi.org/10.1039/C8NJ00221E).
- 22 H. Mohammad Shiri and A. Ehsani, Electrosynthesis of neodymium oxide nanorods and its nanocomposite with conjugated conductive polymer as a hybrid electrode material for highly capacitive pseudocapacitors, *J. Colloid Interface Sci.*, 2017, **495**, 102–110, DOI: [10.1016/j.jcis.2017.01.097](https://doi.org/10.1016/j.jcis.2017.01.097).
- 23 M. Imtiaz, S. Gouadria, A. G. Al-Sehemi and A. Kumar, Enhanced efficiency of the electrode by doping of neodymium on SmFeO<sub>3</sub> for the application of supercapacitor, *Inorg. Chem. Commun.*, 2025, **172**, 113680, DOI: [10.1016/j.inoche.2024.113680](https://doi.org/10.1016/j.inoche.2024.113680).
- 24 J. Sahu, S. Kumar, F. Ahmed, P. A. Alvi, B. Dalela, D. M. Phase, M. Gupta and S. Dalela, Electrochemical and electronic structure properties of high-performance supercapacitor based on Nd-doped ZnO nanoparticles, *J. Energy Storage*, 2023, **59**, 106499, DOI: [10.1016/j.est.2022.106499](https://doi.org/10.1016/j.est.2022.106499).
- 25 S. R. Mishra, V. Chavda, S. Roy, S. Rawat, S. Panda, N. Sarkar, S. K. Khadheer Pasha, M. Ahmaruzzaman and B. M. Nagaraja, Zirconium-based metal-organic frameworks and nanocomposites: Structure-Function correlations in electrochemical applications, *Mater. Today Nano*, 2025, **31**, 100665, DOI: [10.1016/j.mtnano.2025.100665](https://doi.org/10.1016/j.mtnano.2025.100665).
- 26 P. Giri, S. Ganguly and S. Goswami, Appraising the structural and magnetic properties in template assisted neodymium based metal organic frameworks, *Inorg. Chim. Acta*, 2024, **571**, 122245, DOI: [10.1016/j.ica.2024.122245](https://doi.org/10.1016/j.ica.2024.122245).
- 27 L. G. Marazani, M. Gumbo, L. Moyo, B. C. E. Makhubela and G. Mehlena, Synthesis and characterisation of neodymium-based MOFs for application in carbon dioxide reduction to syngas, *New J. Chem.*, 2024, **48**(34), 15025–15035, DOI: [10.1039/D4NJ01420K](https://doi.org/10.1039/D4NJ01420K).
- 28 R. Ramachandran, W. Xuan, C. Zhao, X. Leng, D. Sun, D. Luo and F. Wang, Enhanced electrochemical properties of cerium metal-organic framework based composite electrodes for high-performance supercapacitor application, *RSC Adv.*, 2018, **8**(7), 3462–3469, DOI: [10.1039/C7RA12789H](https://doi.org/10.1039/C7RA12789H).
- 29 Y. Zhang, Q. Xie, R. Shao, J. Ding, J. Liu, W. Xu and Y. Wang, Green synthesis of MOF/CNT gels via in-situ physical mixing strategy toward quasi-solid-state Li-ion hybrid capacitor, *J. Energy Storage*, 2024, **86**, 111156, DOI: [10.1016/j.est.2024.111156](https://doi.org/10.1016/j.est.2024.111156).
- 30 M. Shahbaz, S. Sharif, T. T. Rehman Afzal, S. Shahzad, A. Shahzad, O. Şahin, A. Bentalib, A. Bin Jumah, S. Hussain and N. Ali Khan, Construction of rectangular microporous Cerium 3D metal organic framework for high performance energy storage devices, *J. Solid State Chem.*, 2025, **348**, 125394, DOI: [10.1016/j.jssc.2025.125394](https://doi.org/10.1016/j.jssc.2025.125394).
- 31 S. Sharif, M. Shahbaz, T. T. Rehman Afzal, M. Saeed, A. Shahzad, S. Shahzad, M. N. Asghar, S. Hussain, A. Bentalib and A. B. Jumah, Nitrogen-rich Gadolinium 2D cubic layered metal organic framework for high performance energy storage devices, *Mater. Chem. Phys.*, 2025, **345**, 131279, DOI: [10.1016/j.matchemphys.2025.131279](https://doi.org/10.1016/j.matchemphys.2025.131279).
- 32 H. H. Somaily, Development of Nd doped AlFeO<sub>3</sub> electrode material for supercapacitor applications, *J. Energy Storage*, 2024, **90**, 111958, DOI: [10.1016/j.est.2024.111958](https://doi.org/10.1016/j.est.2024.111958).
- 33 Nonius (2001). *COLLECT. Nonius BV, Delft, The Netherlands*.
- 34 G. M. Sheldrick, *Acta Cryst.*, 2008, **A64**, 112.
- 35 S. K. Ghosh and P. K. Bharadwaj, Self-Assembly of Lanthanide Helicate Coordination Polymers into 3D Metal-Organic Framework Structures, *Inorg. Chem.*, 2004, **43**(7), 2293–2298, DOI: [10.1021/ic034982v](https://doi.org/10.1021/ic034982v).
- 36 J. H. Shah, S. Sharif, M. Shahbaz, M. Saeed, A. Shahzad, S. Farid, S. Shahzad and S. Muhammad, Electrochemical investigation of copper 1D conductive polymer for hybrid supercapacitor applications, *J. Energy Storage*, 2024, **102**, 114058, DOI: [10.1016/j.est.2024.114058](https://doi.org/10.1016/j.est.2024.114058).
- 37 M. Shahbaz, S. Sharif, M. W. Mushtaq, Z. Ghaznavi, Z. Iqbal, M. A. Khurshid, O. Şahin, S. Shahzad, M. Saeed and A. Shahzad, Improved electrochemical performance of nitrogen-containing copper-based 1D metal organic framework derived from highly connective pyridine-2,4,6-tricarboxylic acid for hybrid supercapacitors, *J. Mater. Chem. A*, 2025, **13**(9), 6524–6538, DOI: [10.1039/D4TA05425C](https://doi.org/10.1039/D4TA05425C).
- 38 N. Bhuvanendran, S. Ravichandran, Q. Xu, T. Maiyalagan and H. Su, A quick guide to the assessment of key electrochemical performance indicators for the oxygen reduction reaction: A comprehensive review, *Int. J. Hydrogen Energy*,



- 2022, **47**(11), 7113–7138, DOI: [10.1016/j.ijhydene.2021.12.072](https://doi.org/10.1016/j.ijhydene.2021.12.072).
- 39 K. O. Otun, A. Mukhtar, S. A. Nafiu, I. T. Bello and J. Abdulsalam, Incorporation of redox-activity into metal-organic frameworks for enhanced supercapacitors: A review, *J. Energy Storage*, 2024, **84**, 110673, DOI: [10.1016/j.est.2024.110673](https://doi.org/10.1016/j.est.2024.110673).
- 40 Y. Hao, H. Guo, F. Yang, J. Zhang, N. Wu, M. Wang, C. Li and W. Yang, Hydrothermal synthesis of MWCNT/Ni-Mn-S composite derived from bimetallic MOF for high-performance electrochemical energy storage, *J. Alloys Compd.*, 2022, **911**, 164726, DOI: [10.1016/j.jallcom.2022.164726](https://doi.org/10.1016/j.jallcom.2022.164726).
- 41 C. V. V. Muralee Gopi, D. K. Kulurumotlakatla, K. V. G. Raghavendra, M. Suneetha and R. Ramesh, Hierarchical NiCo<sub>2</sub>O<sub>4</sub>@CuS composite electrode with enhanced surface area for high-performance hybrid supercapacitors, *RSC Adv.*, 2024, **14**(54), 40087–40097, DOI: [10.1039/D4RA07808J](https://doi.org/10.1039/D4RA07808J).
- 42 A. Dhakal, F. A. Perez and S. R. Mishra, Synergetic effect towards high electrochemical performance in LaMnO<sub>3</sub>-Co<sub>3</sub>O<sub>4</sub> composites, *Energy Adv.*, 2025, **4**(1), 162–175, DOI: [10.1039/D4YA00548A](https://doi.org/10.1039/D4YA00548A).
- 43 B. Kirubasankar, P. Palanisamy, S. Arunachalam, V. Murugadoss and S. Angaiah, 2D MoSe<sub>2</sub>-Ni(OH)<sub>2</sub> nanohybrid as an efficient electrode material with high rate capability for asymmetric supercapacitor applications, *Chem. Eng. J.*, 2019, **355**, 881–890, DOI: [10.1016/j.cej.2018.08.185](https://doi.org/10.1016/j.cej.2018.08.185).
- 44 M. K. Singh, A. K. Gupta, S. Krishnan, N. Guha, S. Marimuthu and D. K. Rai, A new hierarchically porous Cu-MOF composited with rGO as an efficient hybrid supercapacitor electrode material, *J. Energy Storage*, 2021, **43**, 103301, DOI: [10.1016/j.est.2021.103301](https://doi.org/10.1016/j.est.2021.103301).
- 45 Y. Sun, X. Du, J. Zhang, N. Huang, L. Yang and X. Sun, Microwave-assisted preparation and improvement mechanism of carbon nanotube@NiMn<sub>2</sub>O<sub>4</sub> core-shell nanocomposite for high performance asymmetric supercapacitors, *J. Power Sources*, 2020, **473**, 228609, DOI: [10.1016/j.jpowsour.2020.228609](https://doi.org/10.1016/j.jpowsour.2020.228609).
- 46 J. H. Shah, M. Shahbaz, S. Sharif, G. Ullah, S. Shahzad, K. S. Munawar, O. Şahin, K. Yusuf and H. Ahmad, Redox active cobalt based bi-linker metal organic frameworks derived from 5-sulfoisophthalic acid and 4,4-bipyridine for supercapacitor, *Mater. Res. Bull.*, 2025, **181**, 113123, DOI: [10.1016/j.materresbull.2024.113123](https://doi.org/10.1016/j.materresbull.2024.113123).
- 47 M. Saeed, J. H. Shah, S. Sharif, M. Shahbaz, G. Ullah, A. Shahzad, Z. S. Şahin, A. Bentalib, S. Hussain and A. B. Jumah, Nitrogen and sulfur-rich cobalt complex for hybrid supercapacitor applications, *Inorg. Chem. Commun.*, 2025, **182**, 115487, DOI: [10.1016/j.inoche.2025.115487](https://doi.org/10.1016/j.inoche.2025.115487).
- 48 A. Khizar, M. Z. Iqbal, A. Zakir, M. Shaheen, S. M. Wabaidur and M. M. Faisal, Synergistic effects of a copper-cobalt-nitroisophthalic acid/neodymium oxide composite on the electrochemical performance of hybrid supercapacitors, *RSC Adv.*, 2024, **14**(14), 10120–10130, DOI: [10.1039/D4RA01719F](https://doi.org/10.1039/D4RA01719F).
- 49 S. Wen, Y. Liu, F. Zhu, R. Shao and W. Xu, Hierarchical MoS<sub>2</sub> nanowires/NiCo<sub>2</sub>O<sub>4</sub> nanosheets supported on Ni foam for high-performance asymmetric supercapacitors, *Appl. Surf. Sci.*, 2018, **428**, 616–622, DOI: [10.1016/j.apsusc.2017.09.189](https://doi.org/10.1016/j.apsusc.2017.09.189).
- 50 K. Ariyoshi, Z. Siroma, A. Mineshige, M. Takeno, T. Fukutsuka, T. Abe and S. Uchida, Electrochemical Impedance Spectroscopy Part 1: Fundamentals, *Electrochemistry*, 2022, **90**(10), 22–66071, DOI: [10.5796/electrochemistry.22-66071](https://doi.org/10.5796/electrochemistry.22-66071).
- 51 M. Shahzad, F. Ahmad, M. Ibraheem, A. Shakoore, S. M. Ramay, M. R. Raza and S. Atiq, Tuning diffusion coefficient, ionic conductivity, and transference number in rGO/BaCoO<sub>3</sub> electrode material for optimized supercapacitor energy storage, *RSC Adv.*, 2025, **15**(8), 6308–6323, DOI: [10.1039/D4RA08894H](https://doi.org/10.1039/D4RA08894H).
- 52 S. D. Alahmari, T. Zahra and M. Ali, Effect of Nd doping on the Physical and electrochemical properties of MnTiO<sub>3</sub> nanoparticles for supercapacitor applications, *J. Alloys Compd.*, 2025, **1010**, 178028, DOI: [10.1016/j.jallcom.2024.178028](https://doi.org/10.1016/j.jallcom.2024.178028).
- 53 R. Siddiqui, M. Rani, A. Ibrahim, A. A. Shah, A. Razaq, S. Bano and M. Ajmal Khan, Enhanced specific capacitance of supercapacitors using wide band gap NdCrO<sub>3</sub> and NdCrO<sub>3</sub>/graphene oxide nanocomposites, *J. Rare Earths*, 2025, **43**(10), 2231–2237, DOI: [10.1016/j.jre.2024.08.023](https://doi.org/10.1016/j.jre.2024.08.023).
- 54 A. Qayyum, M. O. ur Rehman, F. Ahmad, M. A. Khan, S. M. Ramay and S. Atiq, Performance optimization of Nd-doped LaNiO<sub>3</sub> as an electrode material in supercapacitors, *Solid State Ionics*, 2023, **395**, 116227, DOI: [10.1016/j.ssi.2023.116227](https://doi.org/10.1016/j.ssi.2023.116227).
- 55 J. Gu, L. Sun, Y. Zhang, Q. Zhang, X. Li, H. Si, Y. Shi, C. Sun, Y. Gong and Y. Zhang, MOF-derived Ni-doped CoP@C grown on CNTs for high-performance supercapacitors, *Chem. Eng. J.*, 2020, **385**, 123454, DOI: [10.1016/j.cej.2019.123454](https://doi.org/10.1016/j.cej.2019.123454).
- 56 A. H. Anwer, M. Z. Ansari, F. Mashkoore, S. Zhu, M. Shoeb and C. Jeong, Synergistic effect of carbon nanotube and trimetallic MOF nanoarchitecture for electrochemical high-performance asymmetric supercapacitor applications and their charge storage mechanism, *J. Alloys Compd.*, 2023, **955**, 170038, DOI: [10.1016/j.jallcom.2023.170038](https://doi.org/10.1016/j.jallcom.2023.170038).
- 57 Q. Yang, R. Song, Y. Wang, X. Hu, Z. Chen, Z. Li and W. Tan, One-pot synthesis of Zr-MOFs on MWCNTs for high-performance electrochemical supercapacitor, *Colloids Surf., A*, 2021, **631**, 127665, DOI: [10.1016/j.colsurfa.2021.127665](https://doi.org/10.1016/j.colsurfa.2021.127665).
- 58 CCDC 2497615: Experimental Crystal Structure Determination, 2026, DOI: [10.5517/ccdc.csd.cc2ptz7r](https://doi.org/10.5517/ccdc.csd.cc2ptz7r).

